Supplementary Information:

Diverse Quantum Interference Regime in Intramolecular Singlet Fission Chromophores with Thiophene-Based Linkers

Jonghwan Lee[1], Sungsik Eom[1], Hyungjun Kim*[1,2]

[1]Department of Chemistry and Research Institute of Basic Sciences, Incheon National University, Incheon 22012, Republic of Korea

[2]Department of Chemistry, Hanyang University, Seoul 04763, Republic of Korea

e-mail: kim.hyungjun@inu.ac.kr, kimhyungjun@hanyang.ac.kr

Table of Contents

Equilibrium Geometries of Trimethylsilyl-Pentacene (TMS-Pc) Dimer Linked by Thiophene Derivatives

For the Cartesian coordinates of equilibrium structures, please find the attached XYZ files. File names follow the index used in the main text.

Fig. S1 The equilibrium geometries of trimethylsilyl-pentacene (TMS-Pc) dimer linked by thiophene derivatives. Color scheme: hydrogen–white, carbon–gray, oxygen–red, silicon–sky blue, and sulfur–yellow.

Fig. S1 (continued) The equilibrium geometries of trimethylsilyl-pentacene (TMS-Pc) dimer linked by thiophene derivatives. Color scheme: hydrogen–white, carbon–gray, oxygen–red, silicon–sky blue, and sulfur–yellow.
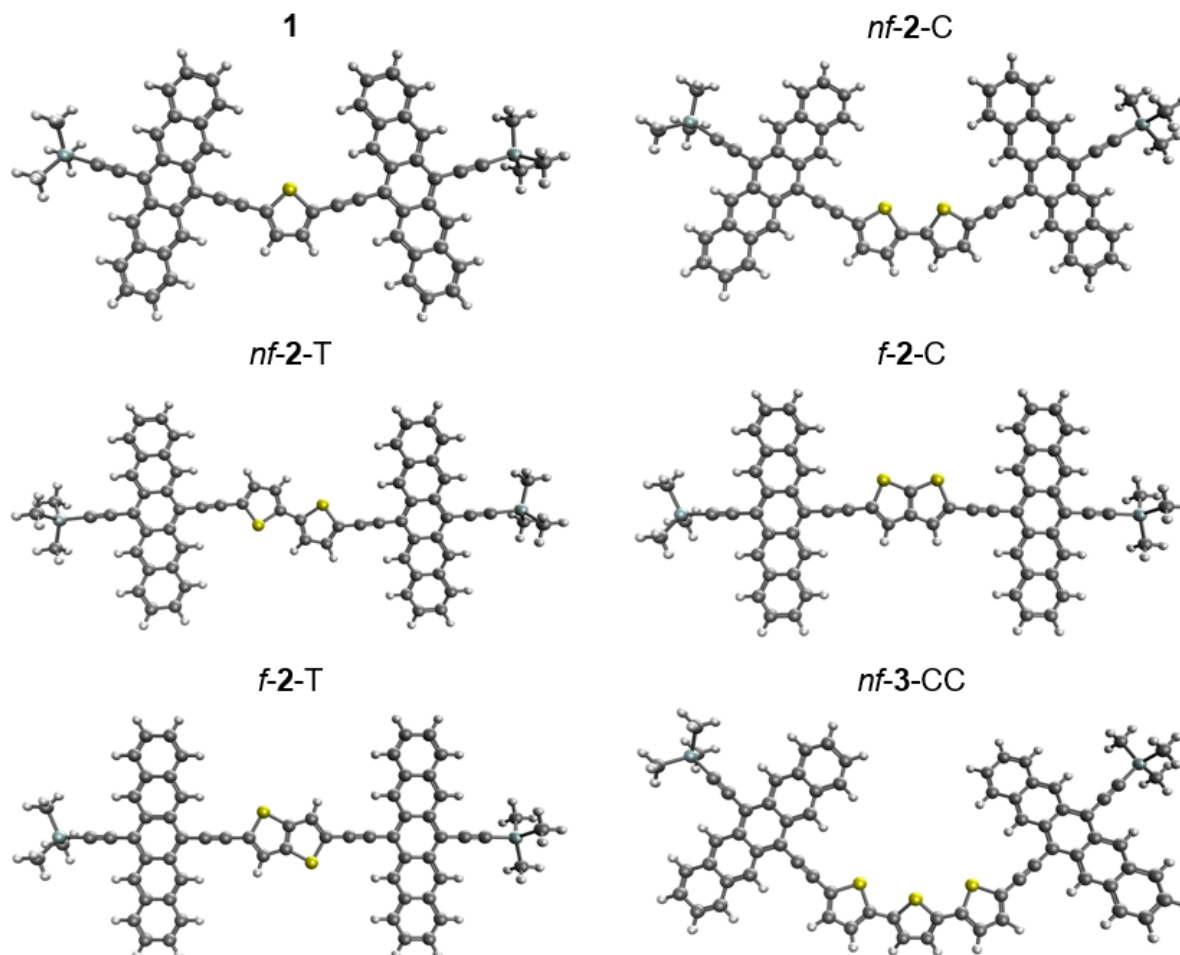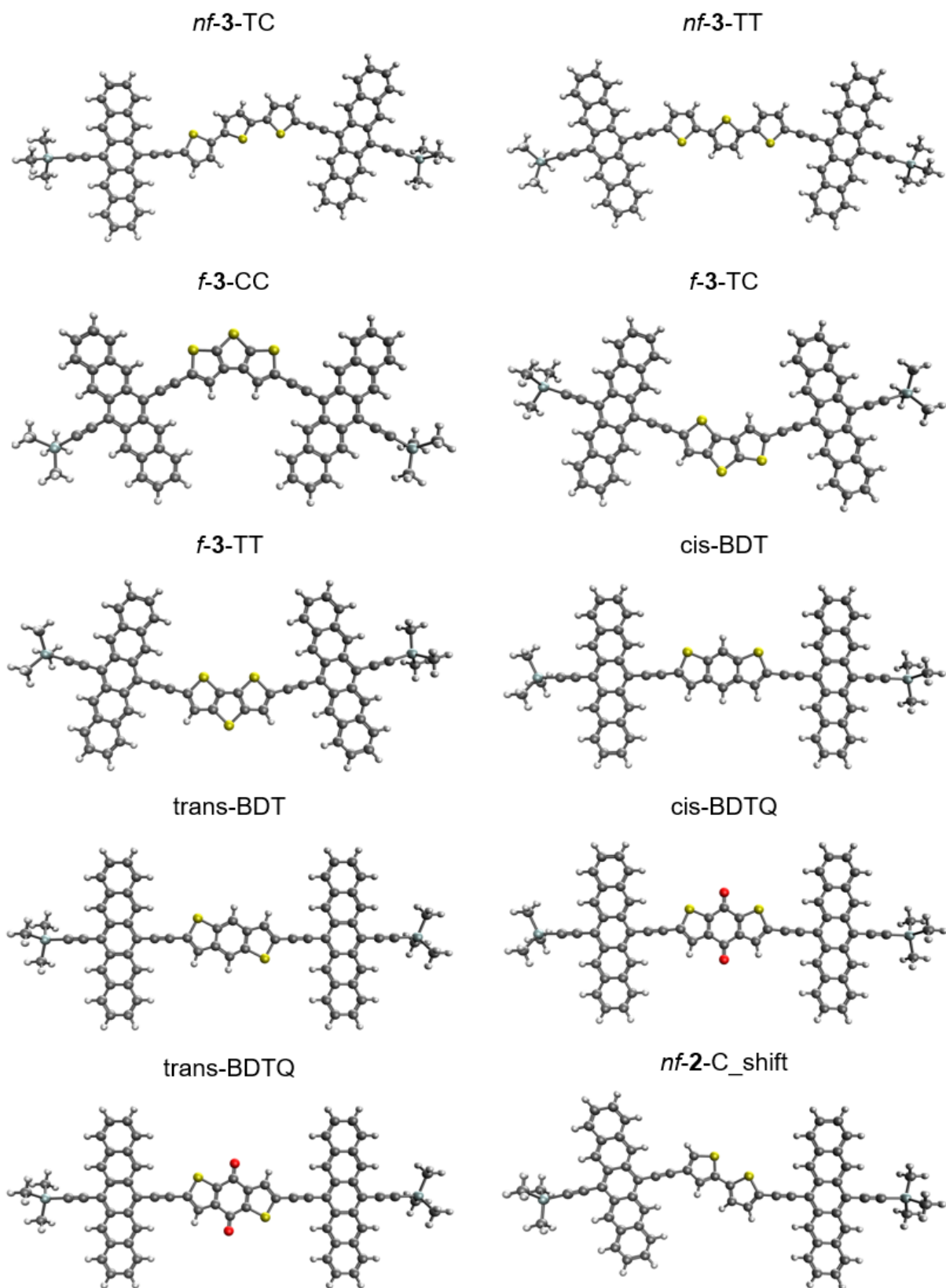
Fig. S1 (continued) The equilibrium geometries of trimethylsilyl-pentacene (TMS-Pc) dimer linked by thiophene derivatives. Color scheme: hydrogen–white, carbon–gray, oxygen–red, silicon–sky blue, and sulfur–yellow.
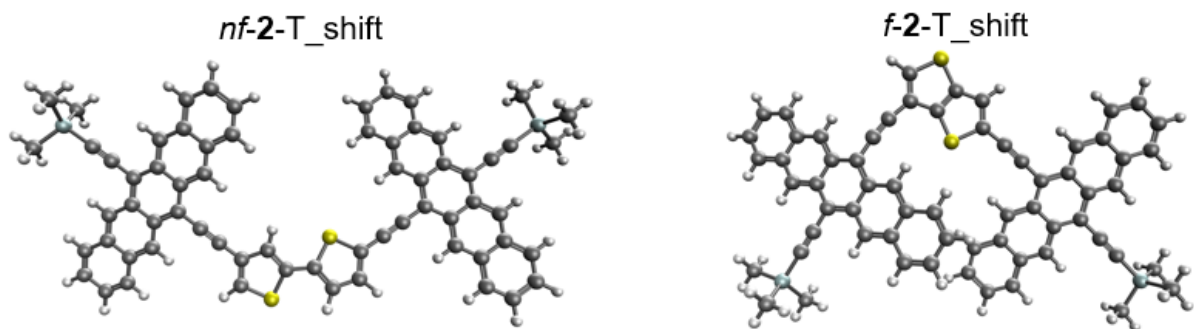
Quantum Chemical Simulation Details

Restricted active space with spin-flip (RAS-SF) calculations

We obtained the ground state equilibrium geometries of trimethylsilyl-pentacene (TMS-Pc) dimers linked via thiophene derivatives using density functional theory (DFT) calculations with the CAM-B3LYP functional[1] and 6-31G(d) basis sets[2-5] in the gas phase. Dispersion interaction was added through Grimme's empirical approach.[6] Restricted active space with double spin-flip (RAS-2SF) calculations were performed to illustrate the energetics relevant to singlet fission (SF). We acquired raw RAS-2SF energies based on the quintet reference state with four electrons in four active orbitals. The derived RAS-2SF energies were refined to achieve the CAM-B3LYP-D/6-31G(d) quality according to the previous report.[7,8] Here is a brief summary of this procedure. First, we performed RAS-2SF calculations and conducted the two-fragment wavefunction decomposition for the SF-relevant excited states, which allows us to quantify the contributions of different diabatic configurations like ground state (GS), local exciton (LE), charge resonance (CR), singlet-singlet (SS) state and triplet-triplet (TT) states to the overall RAS-2SF wavefunctions.

$$\Psi = c_{GS}\psi_{GS} + c_{LE}\psi_{LE} + c_{CR}\psi_{CR} + c_{SS}\psi_{SS} + c_{TT}\psi_{TT}$$

We executed constrained DFT (CDFT) calculations to obtain the charge transfer (CT) energy and compared this to the average energy of the two (or one) lowest RAS-2SF CR adiabatic states to determine the CR energy correction, $E_C[CR]$.[9] Next, we computed the lowest quintet state energy with RAS-2SF and compared it to unrestricted DFT quintet energy to determine the TT energy correction, $E_C[TT]$. Finally, we enforced the energy of RAS-2SF S_2 to be equal to the excitation energy of time-dependent DFT. This gives the LE energy correction, $E_C[LE]$. Combining all the correction terms (E_{raw}), weight factor (ω), and raw RAS-2SF energies (E_{raw}) provides corrected RAS-2SF energies (E_{corr}) which partially recovers dynamic correlation.

$$E_{corr}[\Psi] = E_{raw}[\Psi] + (\omega^{LE} + 2\omega^{SS})E_C[LE] + \omega^{CR}E_C[CR] + \omega^{TT}E_C[TT]$$

However, two-fragmentation scheme is not able to fully capture the contribution of CT between the linker and chromophores, as a portion of the linker and the chromophore are included within the same fragment. To address this limitation and illustrate nonadiabatic coupling between respective states, we have partitioned our model systems into three parts: TMS-Pc (left), linker, and TMS-Pc (right), and performed restricted active space with three spin-flip (RAS-3SF) calculations for three fragments (Fig. S2). We obtained raw RAS-3SF energies based on the septet reference state with six electrons in six active orbitals. All electronic structure calculations were executed using Q-Chem 5.2.[10]

The SF kinetics is theoretically investigated using the three-state model suggested by Krylov et al.[7] This simple scheme has been successfully employed to describe SF kinetics. We are interested in the ME formation (MEF), whose rate could be approximated as below:

$$r_1 = (NAC)^2 e^{-\alpha\beta\Delta E_{MEF}} = (\frac{||\gamma||}{\Delta E})^2 e^{-\alpha\beta\Delta E_{MEF}}$$

where NAC is nonadiabatic coupling estimated by the norm of one-particle transition density matrix ($||\gamma||$) and energy difference between respective states (ΔE) calculated by RAS-3SF, α is a parameter in the free-energy relationship and was set to be 0.5 like in the previous reports.[11,12] β is equal to $1/k_b T$ (k_b is the Boltzmann constant and T is the room temperature of 298 K, and ΔE_{MEF} represents the

difference of RAS-2SF corrected energy between the lowest optically allowed singlet excited state and ME state.

The adiabatic wavefunction is decomposed into diabatic states according to the procedure suggested by Casanova and Krylov.[8] To quantify the contributions of local exciton, charge resonance, and multiexciton states, the overall wavefunction is first expressed as a combination of neutral exciton (NE) and CR configurations. The NE contribution is further split into single LE and simultaneous ME based on whether one or more chromophores are excited. The weights of the LE and CR parts come directly from the amplitudes of those configurations in the total wavefunction. To analyze the ME contribution, spin correlators are employed to distinguish between TT and SS couplings. The trace of the spin correlator matrix gives the overall TT weight, while the off-diagonal elements reveal the specific TT couplings between pairs of chromophores. The remaining ME character is assigned as SS.
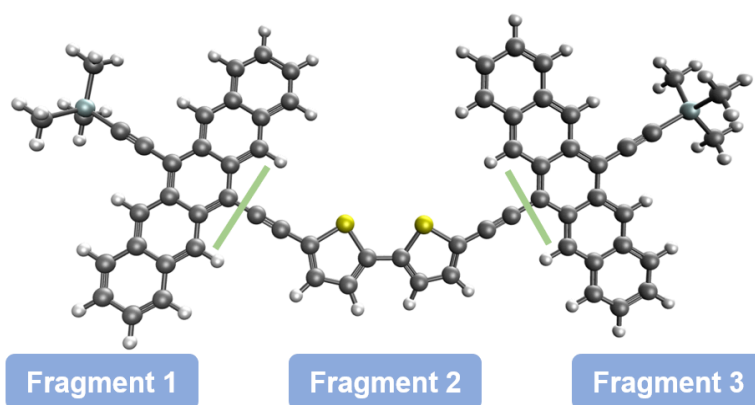

Fig. S2 Example of three fragmentations for *nf*-**2**-C. The green dash lines correspond to the border between the fragments.

Nonequilibrium green's function calculations

We have performed nonequilibrium Green function (NEGF) calculations to describe transmission in molecular junctions. The junctions were constructed using Au (001) lattice as the electrodes, with six layers on each side, and each layer composed of a 3 × 3 array of Au atoms. The equilibrium structures of the *f*-**3** linkers (*f*-**3**-TT, *f*-**3**-TC, and *f*-**3**-CC) were determined using the CAM-B3LYP-D/6-311G(d,p) level of theory. These linkers were then inserted between the gold electrodes, maintaining a distance of 2.75 Å between the linker and each gold layer (Supplementary Fig. 8). The Perdew-Burke-Ernzerhof (PBE) functional was applied with a single-ζ polarized basis set for gold atoms and a double-ζ polarized basis set for other light atoms. The Brillouin zone of the gold electrodes was sampled using a Monkhorst-Pack *k*-point grid of 1 × 1 × 100, while the scattering regions were sampled with a grid of 1 × 1 × 1. The energy cutoff for the real-space grid was set to 200 Ry. We calculated the transmission coefficients for the molecular junctions at zero bias voltage using nonequilibrium Green's function (NEGF) methods, considering an energy range from -2 eV to +3 eV. All calculations relevant to transmission were performed with SIESTA[13] and Gollum[14].

(A) *f*-**3**-TT
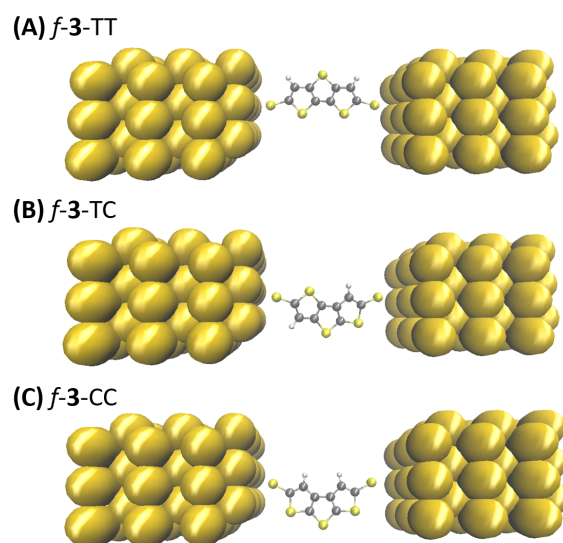
(B) *f*-**3**-TC

(C) *f*-**3**-CC

Fig. S3 The structures of molecular junctions consisting of six Au (001) layers on both sides, with the linkers placed between the gold layers: (A) *f*-**3**-TT, (B) *f*-**3**-TC, (C) *f*-**3**-CC. Color scheme: hydrogen–white, carbon–gray, sulfur–yellow, and gold–yellow brown.

Singlet Fission Kinetics and Relevant Electronic Properties

Table. S1. Nonadiabatic coupling (NAC), energy difference between a multiexciton state and the lowest optically allowed singlet excited state (ΔE_{MEF}), and the logarithm of multiexciton formation rate relative to **1** ($\log(r/r_1)$) for 6,6'-TMS-Pcs attached to thiophene-based linkers.

Index	NAC (eV^{-1})	ΔE_{MEF} (eV)	$\log(r/r_1)$
1	0.39	-0.44	0.00
nf-**2**-T	0.16	-0.47	-0.57
nf-**2**-C	0.17	-0.47	-0.53
f-**2**-T	0.39	-0.44	-0.07
f-**2**-C	0.094	-0.53	-0.48
nf-**3**-TT	0.064	-0.50	-1.12
nf-**3**-TC	0.055	-0.50	-1.21
nf-**3**-CC	0.053	-0.50	-1.25
f-**3**-TT	0.23	-0.46	-0.36
f-**3**-TC	0.052	-0.54	-0.92
f-**3**-CC	0.018	-0.55	-1.78
trans-BDT	0.092	-0.49	-0.89
cis-BDT	0.035	-0.54	-1.26
trans-BDTQ	0.026	-0.50	-1.90
cis-BDTQ	0.084	-0.42	-1.56

Geometric Features and Correlation with Nonadiabatic Coupling

Table. S2 Distance between each terminal chromophore and linker (d_{Pc1-L} and d_{Pc2-L}), the total distance between two terminal chromophores via a linker ($d_{Pc1-L-Pc2}$), the distance between two terminal chromophores (d_{Pc-Pc}), in-plane angle (θ), and dihedral angle (φ). Distances were measured between the centers of mass of each fragment. Graphical description of each geometric feature can be found in Supplementary Fig. 2.

Index	d_{Pc1-L} (Å)	d_{Pc2-L} (Å)	$d_{Pc1-L-Pc2}$ (Å)	d_{Pc-Pc} (Å)	θ (°)	φ (°)
1	6.65	6.65	13.3	13.0	15.0	0.2
nf-**2**-T	8.55	8.55	17.1	17.1	14.3	8.7
nf-**2**-C	8.40	8.40	16.8	15.8	61.8	16.9
f-**2**-T	7.75	7.75	15.5	15.5	0.0	0.0
f-**2**-C	7.78	7.79	15.6	15.5	3.1	0.1
nf-**3**-TT	10.5	10.5	21.0	20.8	30.6	0.3
nf-**3**-TC	10.2	10.4	20.6	20.4	20.5	6.8
nf-**3**-CC	9.96	9.96	19.9	17.8	87.3	24.4
f-**3**-TT	8.63	8.63	17.3	16.9	30.8	0.3
f-**3**-TC	8.53	8.79	17.3	16.6	35.2	0.1
f-**3**-CC	8.71	8.71	17.4	15.6	57.3	3.7
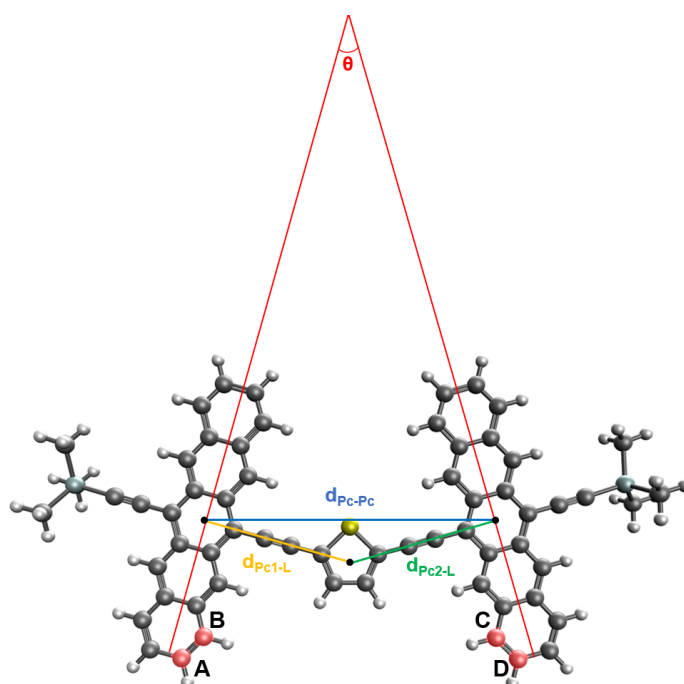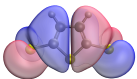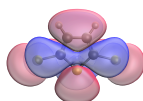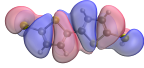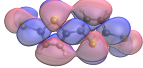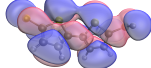
Fig. S4 Graphical illustration of four geometric features mentioned in Table S2.

Energy Level and Spatial Distribution of Frontier Molecular Orbital

Table. S3 HOMO energy (HOMO), LUMO energy (LUMO), HOMO and LUMO offset between the linker and TMS-Pc chromophore (Offset$_{HOMO}$ and Offset$_{LUMO}$), and the minimum of offsets (Offset$_{min}$). All energies are given in eV.

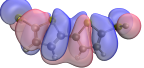| Index	HOMO	LUMO	Offset$_{HOMO}$	Offset$_{LUMO}$	Offset$_{min}$
1	-8.12	-0.87	2.13	1.15	1.15
nf-**2**-T	-7.11	-0.26	1.12	1.75	1.12
nf-**2**-C	-7.30	-0.05	1.31	1.97	1.31
f-**2**-T	-7.51	0.33	1.52	2.34	1.52
f-**2**-C	-7.64	0.63	1.65	2.64	1.65
nf-**3**-TT	-6.84	-0.58	0.84	1.43	0.84
nf-**3**-TC	-6.90	-0.52	0.91	1.50	0.91
nf-**3**-CC	-6.92	-0.47	0.93	1.54	0.93
f-**3**-TT	-7.23	-0.08	1.24	1.93	1.24
f-**3**-TC	-7.31	0.30	1.31	2.31	1.31
f-**3**-CC	-7.41	0.45	1.42	2.47	1.42

Index	HOMO	LUMO
1		
nf-**2**-T		
nf-**2**-C		
f-**2**-T		

f-**2**-C		
nf-**3**-TT		
nf-**3**-TC		
nf-**3**-CC		
f-**3**-TT		
f-**3**-TC		
f-**3**-CC		

Fig. S5 Spatial distribution of molecular orbitals from LUMO to HOMO of diverse thiophene-based linkers. Isovalue of 0.02 Å^{-3}.

Extended Curly Arrow Rules

Curly arrow notation is a fundamental tool in organic chemistry used to depict electron movement during chemical reactions. This notation was introduced in the 1920s and further developed in the 1930s, with different symbols for electron pairs and single electrons.[15-18] Recent quantum chemical descriptions have provided a rigorous foundation for curly arrows using dynamic Voronoi metropolis sampling.[19] Curly arrow rules (CARs) were developed to predict electron transmission in molecular electronic devices.[20,21] These rules state that for alternant hydrocarbons, electron transmission is possible if electron displacement can be drawn using curly arrows in a resonance structure. The theoretical foundation for CARs is related to the preferential flow of electrons through bonds with more double bond character. Under certain conditions, the transmission probability near the Fermi level is proportional to the square of the Pauling bond order.[20,21] CARs provide a simple method for predicting quantum interference effects without complex calculations. However, CARs have limitations, particularly for molecules with cross-conjugation and heteroatoms.[22] Examples of CARs breakdown include anthraquinone isomers[23] and methoxy-substituted meta-connected oligo(phenylene-ethylene) wires[24]. To address these shortcomings, extended curly arrow rules (ECARs) were introduced.[22] ECARs take into account electron-withdrawing groups (EWGs) and electron-donating groups (EDGs) in molecular structures. These extended rules provide guidelines that predict constructive quantum interference (CQI), destructive quantum interference (DQI), or shifted destructive quantum interference (SDQI) (see below). ECARs successfully predict behavior in cases where CARs fail, such as anthraquinone isomers and methoxy-substituted OPE wires. The extended rules have been applied to diverse molecular systems, including polycyclic aromatics with heteroatoms,[25] odd-membered rings,[26] and non-alternant hydrocarbons.[27] ECARs have successfully explained conductance behavior in benzodithiophene derivatives[28] and diketopyrrolopyrrole-based molecular switches.[29] The rules can be applied to acyclic pathways[30] and fulvenes,[31] demonstrating their versatility. The extended rules have shown effectiveness in predicting quantum interference behavior in cross-conjugated molecules and polycyclic aromatic with heteroatoms. Overall, ECARs represent an improvement over CARs, offering a more comprehensive approach to predicting electron transmission in diverse molecular structures.

The rules are summarized below:

1. Replace one chromophore moiety with a donor group (D) and the other with an acceptor group (A). If you can draw curly arrows to transfer the D lone pair onto A, CQI is expected. If not, DQI is expected.
2. If DQI is expected in rule 1, check if the molecule contains electron withdrawing groups (EWGs) or electron donating groups (EDGs).
3. If EWGs, replace chromophore moieties with D groups. If a lone pair from each D can be independently transferred to the same EWG, SDQI is expected.
4. If EDGs, replace chromophore moieties with A groups. If a lone pair from the same EDG can be independently transferred to each A group, SDQI is expected.
5. Otherwise, DQI is expected.

Inspection of an Expanded Array of Thiophene Derivatives

(A) trans-BDT : CQI
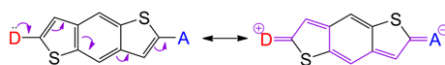
(B) cis-BDT : SDQI
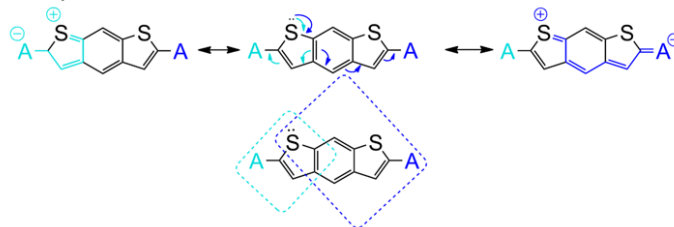
(C) trans-BDTQ : DQI
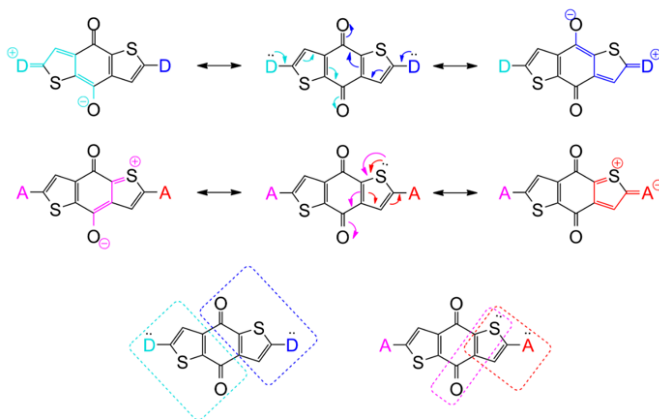
(D) cis-BDTQ : SDQI
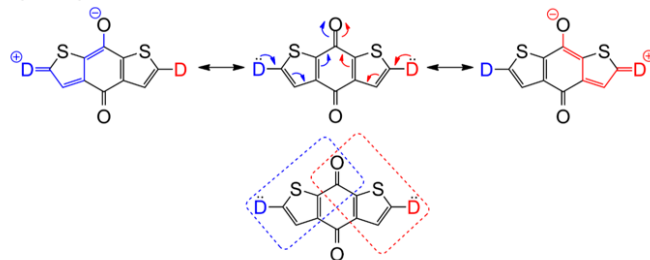
Fig. S6 Applications of extended curly arrow rules to (A) trans-BDT, (B) cis-BDT, (C) trans-BDTQ, and (D) cis-BDTQ.

Results for 6,6'-TMS-Tetracene and 2,2'-TMS-Pentacene
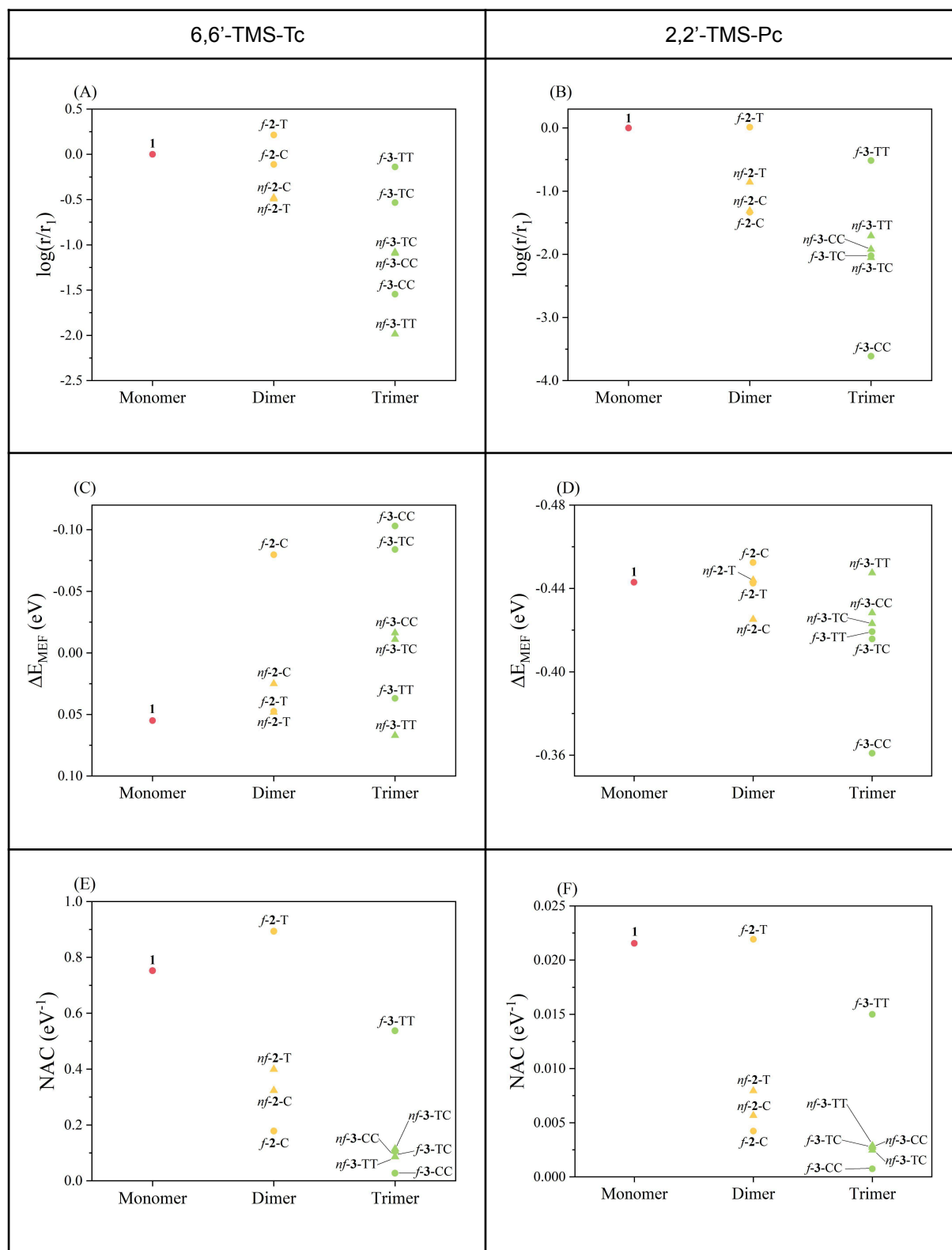
Fig. S7 (A,B) Logarithm of multiexciton formation rates relative to **1**, (C,D) thermodynamic driving force for multiexciton formation (ΔE_{MEF}), (E,F) nonadiabatic coupling (NAC) of chromophores having nonfused thiophene chains (triangles) and fused thiophene derivatives (circles) as a function of the

number of repeating units. Color scheme: Monomer (red), dimer (orange), and trimer (green). (A,C,E) for 6,6'-TMS-Tc and (B,D,F) for 2,2'-TMS-Pc dimers.

Table. S4 Nonadiabatic coupling (NAC), energy difference between a multiexciton state and the lowest optically allowed singlet excited state (ΔE_{MEF}), and the logarithm of multiexciton formation rate relative to **1** for 6,6'-TMS-Tcs attached to thiophene-based linkers.

Index	NAC (eV^{-1})	ΔE_{MEF} (eV)	log(r/r$_1$)
1	0.753	0.055	0.00
nf-**2**-T	0.399	0.048	-0.49
nf-**2**-C	0.324	0.025	-0.48
f-**2**-T	0.893	0.047	0.21
f-**2**-C	0.178	-0.080	-0.11
nf-**3**-TT	0.086	0.067	-1.98
nf-**3**-TC	0.114	-0.011	-1.08
nf-**3**-CC	0.107	-0.016	-1.09
f-**3**-TT	0.537	0.037	-0.14
f-**3**-TC	0.105	-0.084	-0.53
f-**3**-CC	0.027	-0.103	-1.54

Table. S5 Nonadiabatic coupling (NAC), energy difference between a multiexciton state and the lowest optically allowed singlet excited state (ΔE_{MEF}), and the logarithm of multiexciton formation rate relative to **1** for 2,2'-TMS-Pcs attached to thiophene-based linkers.

| Index	NAC (eV^{-1})	ΔE_{MEF} (eV)	log(r/r$_1$)
1	0.022	-0.443	0.00
nf-**2**-T	0.008	-0.444	-0.86
nf-**2**-C	0.006	-0.425	-1.31
f-**2**-T	0.022	-0.443	0.01
f-**2**-C	0.004	-0.452	-1.34
nf-**3**-TT	0.003	-0.447	-1.71
nf-**3**-TC	0.002	-0.423	-2.05
nf-**3**-CC	0.003	-0.428	-1.92
f-**3**-TT	0.015	-0.419	-0.52
f-**3**-TC	0.003	-0.416	-2.02

t-**3**-CC	0.001	-0.361	-3.61

Impact of Linkage Site Shifting

Table. S6 Nonadiabatic coupling (NAC), energy difference between a multiexciton state and the lowest optically allowed singlet excited state (ΔE_{MEF}), and logarithm of multiexciton formation rate relative to **1** ($\log(r/r_1)$) upon shifting chromophore attachment sites.

Index	Before shifting			After shifting		
	NAC (eV^{-1})	ΔE_{MEF} (eV)	$\log(r/r_1)$	NAC (eV^{-1})	ΔE_{MEF} (eV)	$\log(r/r_1)$
nf-**2**-T	0.16	-0.466	-0.57	0.03	-0.546	-1.28
nf-**2**-C	0.17	-0.467	-0.53	0.02	-0.550	-1.81
f-**2**-T	0.39	-0.438	-0.07	0.05	-0.533	-1.08

Wavefunction Decomposition Analysis

Table. S7 Excitation energies, oscillator strength, and adiabatic wavefunction composition of the lowest optically allowed singlet excited state.

Index	E_{raw} (eV)	f (a.u.)	GS (%)	LE (%)	CR (%)	SS (%)	TT (%)	ME for 3 fragments (%)
1	3.05	2.25	0.0	15.2	35.8	47.7	0.8	0.6
nf-**2**-T	3.24	1.52	0.0	18.2	23.1	35.2	23.1	0.4
nf-**2**-C	3.22	1.02	0.0	9.9	24.7	36.3	28.4	0.6
f-**2**-T	3.00	2.98	0.0	14.4	37.5	46.6	0.4	1.1
f-**2**-C	3.33	1.90	0.0	30.9	14.3	53.2	1.0	0.7
nf-**3**-TT	3.35	2.38	0.0	21.5	10.0	67.2	0.1	1.3
nf-**3**-TC	3.38	2.22	0.0	21.6	8.4	68.7	0.0	1.2
nf-**3**-CC	3.39	1.38	0.0	21.3	8.0	69.5	0.0	1.2
f-**3**-TT	3.13	2.64	0.0	26.1	26.8	46.3	0.5	0.5
f-**3**-TC	3.30	1.70	0.0	33.8	14.1	51.2	0.4	0.5
f-**3**-CC	3.47	1.40	0.0	24.3	5.0	69.0	0.0	1.6

E_{raw}: Uncorrected RAS-3SF excitation energies, f: oscillator strength, GS: ground state, LE: local exciton, CR: charge resonance, SS: singlet-singlet multiexciton, TT: triplet-triplet multiexciton, ME for 3 fragments: multiexcitons for the whole fragments

Table. S8 Excitation energies, oscillator strength, and adiabatic wavefunction composition of the adiabatic state with a dominant multiexciton triplet-triplet character.

Index	E_{raw} (eV)	f (a.u.)	GS (%)	LE (%)	CR (%)	SS (%)	TT (%)	ME for 3 fragments (%)
1	2.02	0.00	0.0	0.2	19.3	-1.2	80.7	1.1
nf-**2**-T	2.15	0.00	0.0	0.8	8.3	-0.6	90.0	1.5
nf-**2**-C	2.16	0.00	0.0	0.1	7.5	-0.5	91.4	1.5
f-**2**-T	2.04	0.00	0.0	0.2	17.9	-1.2	81.2	1.9
f-**2**-C	2.18	0.00	0.0	0.0	5.6	-0.2	92.2	2.4
nf-**3**-TT	2.20	0.00	0.0	0.0	2.2	-0.1	96.3	1.6
nf-**3**-TC	2.20	0.00	0.0	0.0	2.0	-0.1	96.4	1.7
nf-**3**-CC	2.20	0.00	0.0	0.0	1.9	0.0	96.4	1.8

Index	E_{raw} (eV)	f (a.u.)	GS (%)	LE (%)	CR (%)	SS (%)	TT (%)	ME for 3 fragments (%)
f-3-TT	2.13	0.00	0.0	1.0	10.4	-0.7	87.8	1.5
f-3-TC	2.18	0.00	0.0	0.0	5.4	-0.3	93.2	1.7
f-3-CC	2.19	0.00	0.0	0.0	2.9	-0.1	93.8	3.4

E_{raw}: Uncorrected RAS-3SF excitation energies, f: oscillator strength, GS: ground state, LE: local exciton, CR: charge resonance, SS: singlet-singlet multiexciton, TT: triplet-triplet multiexciton, ME for 3 fragments: multiexcitons for the whole fragments

Table. S9 Excitation energies, oscillator strength, and adiabatic wavefunction composition of the adiabatic state with a dominant charge resonance character.

Index	E_{raw} (eV)	f (a.u.)	GS (%)	LE (%)	CR (%)	SS (%)	TT (%)	ME for 3 fragments (%)
1	4.08	0.00	0.0	5.4	68.5	22.6	3.0	0.6
nf-2-T	4.31	0.18	0.0	27.0	48.5	22.4	1.3	0.8
	4.62	0.00	0.0	17.8	49.0	-8.2	40.8	0.5
nf-2-C	4.32	0.16	0.0	3.4	51.1	42.3	1.4	1.7
	4.61	0.00	0.0	2.8	59.4	-2.2	39.5	0.5
f-2-T	4.05	0.00	0.0	6.8	63.5	25.6	3.0	1.1
f-2-C	4.45	0.00	0.0	2.7	80.9	13.3	1.4	1.7
	4.73	0.09	0.0	2.8	70.8	8.9	17.0	0.4
nf-3-TT	N/A[a]							
nf-3-TC	4.49	0.89	0.0	6.0	41.9	46.2	0.4	5.5
	4.80	0.00	0.0	0.5	48.8	-19.6	69.6	0.7
nf-3-CC	4.52	0.82	0.0	5.3	47.4	41.7	0.5	5.2
	4.79	0.00	0.0	0.5	65.5	-10.2	43.5	0.7
f-3-TT	4.18	0.14	0.0	17.5	58.9	21.0	1.8	0.8
f-3-TC	4.54	0.08	0.0	1.0	89.8	6.4	1.1	1.6
	4.68	0.13	0.0	1.0	83.1	10.2	5.2	0.5
f-3-CC	4.77	0.00	0.0	0.2	93.4	1.2	2.7	2.6
	4.85	0.00	0.0	0.5	90.0	0.9	8.0	0.6

E_{raw}: Uncorrected RAS-3SF excitation energies, f: oscillator strength, GS: ground state, LE: local exciton, CR: charge resonance, SS: singlet-singlet multiexciton, TT: triplet-triplet multiexciton, ME for 3 fragments: multiexcitons for the whole fragments

a) After examining the first ten excited states of the system, which span an excitation energy range of 4.21 eV, we were unable to identify any electronic state exhibiting a dominant charge resonance character. This suggests that the charge resonance states, if present, may lie at higher excitation energies.

Electron-Hole Correlation Diagram

To quantify the contribution of CT character in the S_1 state, we employed a sophisticated fragment-based excited state analysis using time-dependent density functional theory (TDDFT), focusing on the one-electron transition (1TDM) between the ground and S_1 state. 1TDM can be expressed as

$$\gamma_{0I}(r_h, r_e) = n \int \dots \int \Psi_0(r_h, r_2, \dots, r_n) \Psi_I(r_e, r_2, \dots, r_n) dr_2 \dots dr_n$$

where Ψ_0 and Ψ_I represent the ground and excited state wavefunctions, respectively, and r_h and r_e denote the coordinates of the hole and electron derived from Ψ_0 and Ψ_I. Utilizing the equation for $\gamma_{0I}(r_h, r_e)$, we can quantify the contribution of CT diabats, defined as

$$\Omega_{AB} = \int_A \int_B |\gamma_{0I}(r_h, r_e)|^2 dr_e dr_h$$

where the hole is confined to fragment *A* of the system and the electron to another fragment *B*. The resulting Ω-matrix, comprised of all calculated Ω_{AB} values, can be visualized as a pseudocolor matrix plot, commonly referred to as an Ω-plot or electron-hole correlation plot. These plots depict the electron-hole correlation for the lowest optically allowed singlet state of the TMS-Pc dimers connected by thiophene-based linkers investigated in this study. Time-dependent density functional theory calculations with CAM-B3LYP-D functional and 6-31G(d) basis sets were conducted. Rectangular boxes represent electron-hole correlation between three fragments: TMS-Pc, linker, and TMS-Pc (from left to right, and from bottom to top). To better highlight the variations of CT between the chromophores and linkers, the color scale in the plots has been intentionally limited to a range of 0.0 to 0.1. This choice of scale leads to a uniform appearance of the LE contribution on each part of the TMS-Pc chromophores, despite the difference in their actual LE contributions. By focusing on this narrower color range, the plots effectively emphasize the relative changes in CT contributions across the different linkers. These plots clearly reveal an increase CT contributions between the chromophores and the linkers as the number of trans S atoms in the linker increases.

Electron-hole correlation diagram was generated using TheoDORE.[32]
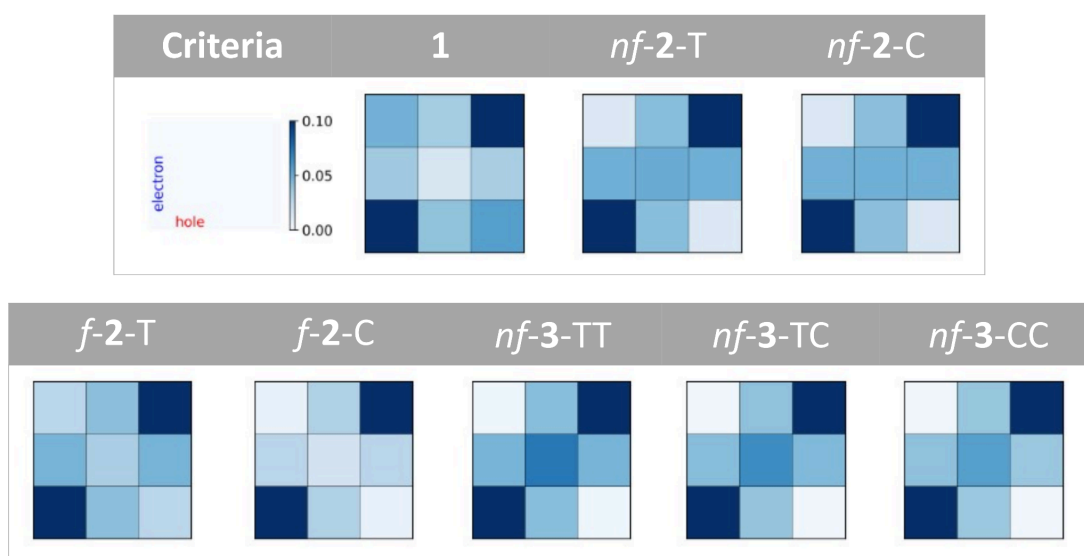

Fig. S8 Electron-hole correlation diagrams within the lowest optically allowed singlet state for the TMS-Pc dimers connected via thiophene-based linkers investigated in this work.

Reference

1   T. Yanai, D. P. Tew and N. C. Handy, *Chem. Phys. Lett.*, 2004, **393**, 51–57.

2   W. J. Hehre, R. Ditchfield and J. A. Pople, *J. Chem. Phys.*, 1972, **56**, 2257–2261.

3   J. S. Binkley, J. A. Pople and W. J. Hehre, *J. Am. Chem. Soc.*, 1980, **102**, 939–947.

4   M. M. Francl, W. J. Pietro, W. J. Hehre, J. S. Binkley, M. S. Gordon, D. J. DeFrees and J. A. Pople, *J. Chem. Phys.*, 1982, **77**, 3654–3665.

5   V. A. Rassolov, J. A. Pople, M. A. Ratner and T. L. Windus, *J. Chem. Phys.*, 1998, **109**, 1223–1229.

6   S. Grimme, *J. Comput. Chem.*, 2006, **27**, 1787–1799.

7   M. H. Farag and A. I. Krylov, *J. Phys. Chem. C*, 2018, **122**, 25753–25763.

8   D. Casanova and A. I. Krylov, *J. Chem. Phys.*, 2016, **144**, 014102.

9   B. Kaduk, T. Kowalczyk and T. Van Voorhis, *Chem. Rev.*, 2012, **112**, 321–370.

10   Y. Shao, Z. Gan, E. Epifanovsky, A. T. B. Gilbert, M. Wormit, J. Kussmann, A. W. Lange, A. Behn, J. Deng, X. Feng, D. Ghosh, M. Goldey, P. R. Horn, L. D. Jacobson, I. Kaliman, R. Z. Khaliullin, T. Kuś, A. Landau, J. Liu, E. I. Proynov, Y. M. Rhee, R. M. Richard, M. A. Rohrdanz, R. P. Steele, E. J. Sundstrom, H. L. Woodcock, P. M. Zimmerman, D. Zuev, B. Albrecht, E. Alguire, B. Austin, G. J. O. Beran, Y. A. Bernard, E. Berquist, K. Brandhorst, K. B. Bravaya, S. T. Brown, D. Casanova, C.-M. Chang, Y. Chen, S. H. Chien, K. D. Closser, D. L. Crittenden, M. Diedenhofen, R. A. DiStasio, H. Do, A. D. Dutoi, R. G. Edgar, S. Fatehi, L. Fusti-Molnar, A. Ghysels, A. Golubeva-Zadorozhnaya, J. Gomes, M. W. D. Hanson-Heine, P. H. P. Harbach, A. W. Hauser, E. G. Hohenstein, Z. C. Holden, T.-C. Jagau, H. Ji, B. Kaduk, K. Khistyaev, J. Kim, J. Kim, R. A. King, P. Klunzinger, D. Kosenkov, T. Kowalczyk, C. M. Krauter, K. U. Lao, A. D. Laurent, K. V. Lawler, S. V. Levchenko, C. Y. Lin, F. Liu, E. Livshits, R. C. Lochan, A. Luenser, P. Manohar, S. F. Manzer, S.-P. Mao, N. Mardirossian, A. V. Marenich, S. A. Maurer, N. J. Mayhall, E. Neuscamman, C. M. Oana, R. Olivares-Amaya, D. P. O'Neill, J. A. Parkhill, T. M. Perrine, R. Peverati, A. Prociuk, D. R. Rehn, E. Rosta, N. J. Russ, S. M. Sharada, S. Sharma, D. W. Small, A. Sodt, T. Stein, D. Stück, Y.-C. Su, A. J. W. Thom, T. Tsuchimochi, V. Vanovschi, L. Vogt, O. Vydrov, T. Wang, M. A. Watson, J. Wenzel, A. White, C. F. Williams, J. Yang, S. Yeganeh, S. R. Yost, Z.-Q. You, I. Y. Zhang, X. Zhang, Y. Zhao, B. R. Brooks, G. K. L. Chan, D. M. Chipman, C. J. Cramer, W. A. Goddard, M. S. Gordon, W. J. Hehre, A. Klamt, H. F. Schaefer, M. W. Schmidt, C. D. Sherrill, D. G. Truhlar, A. Warshel, X. Xu, A. Aspuru-Guzik, R. Baer, A. T. Bell, N. A. Besley, J.-D. Chai, A. Dreuw, B. D. Dunietz, T. R. Furlani, S. R. Gwaltney, C.-P. Hsu, Y. Jung, J. Kong, D. S. Lambrecht, W. Liang, C. Ochsenfeld, V. A. Rassolov, L. V. Slipchenko, J. E. Subotnik, T. Van Voorhis, J. M. Herbert, A. I. Krylov, P. M. W. Gill and M. Head-Gordon, *Mol. Phys.*, 2015, **113**, 184–215.

11   X. Feng, A. B. Kolomeisky and A. I. Krylov, *J. Phys. Chem. C*, 2014, **118**, 19608–19617.

12   X. Feng and A. I. Krylov, *Phys. Chem. Chem. Phys.* 2016, **18**, 7751-7761.

13   J. M. Soler, E. Artacho, J. D. Gale, A. García, J. Junquera, P. Ordejón and D. Sánchez-Portal, *J. Phys.: Condens. Matter*, 2002, **14**, 2745–2779.

14   J. Ferrer, C. J. Lambert, V. M. García-Suárez, D. Z. Manrique, D. Visontai, L. Oroszlany, R. Rodríguez-Ferradás, I. Grace, S. W. D. Bailey, K. Gillemot, H. Sadeghi and L. A. Algharagholy, *New. J. Phys.*, 2014, **16**, 093029.

15   W. O. Kermack and R. Robinson, *J. Chem. Soc., Trans.*, 1922, **121**, 427–440.

16   D. O'Hagan and D. Lloyd, *Chem. World*, 2010, **7**, 54–57.

17   C. K. Ingold, *Chem. Rev.*, 1934, **15**, 225–274.

18   G. Spiteller, *Angew. Chem.*, 1965, **77**, 228–228.

19   Y. Liu, P. Kilby, T. J. Frankcombe and T. W. Schmidt, *Nat. Commun.*, 2018, **9**, 1436.

20   T. Stuyver, S. Fias, F. De Proft and P. Geerlings, *J. Phys. Chem. C*, 2015, **119**, 26390–26400.

21   T. Stuyver, N. Blotwijk, S. Fias, P. Geerlings and F. De Proft, *ChemPhysChem*, 2017, **18**, 3012–3022.

22   L. J. O'Driscoll and M. R. Bryce, *Nanoscale*, 2021, **13**, 1103–1123.

23   J. Alqahtani, H. Sadeghi, S. Sangtarash and C. J. Lambert, *Angew. Chem., Int. Ed.*, 2018, **57**, 15065–15069.

24   F. Jiang, D. I. Trupp, N. Algethami, H. Zheng, W. He, A. Alqorashi, C. Zhu, C. Tang, R. Li, J. Liu, H. Sadeghi, J. Shi, R. Davidson, M. Korb, A. N. Sobolev, M. Naher, S. Sangtarash, P. J. Low, W. Hong and C. J. Lambert, *Angew. Chem., Int. Ed.*, 2019, **58**, 18987–18993.

25   S. Sangtarash, H. Sadeghi and C. J. Lambert, *Phys. Chem. Chem. Phys.*, 2018, **20**, 9630–9637.

26   A. Alanazy, E. Leary, T. Kobatake, S. Sangtarash, M. T. González, H.-W. Jiang, G. R. Bollinger, N. Agräit, H. Sadeghi, I. Grace, S. J. Higgins, H. L. Anderson, R. J. Nichols and C. J. Lambert, *Nanoscale*, 2019, **11**, 13720–13724.

27   J. Xia, B. Capozzi, S. Wei, M. Strange, A. Batra, J. R. Moreno, R. J. Amir, E. Amir, G. C. Solomon, L. Venkataraman and L. M. Campos, *Nano Lett.*, 2014, **14**, 2941–2945.

28   Y. Zhang, G. Ye, S. Soni, X. Qiu, T. L. Krijger, H. T. Jonkman, M. Carlotti, E. Sauter, M. Zharnikov and R. C. Chiechi, *Chem. Sci.*, 2018, **9**, 4414–4423.

29   Y.-P. Zhang, L.-C. Chen, Z.-Q. Zhang, J.-J. Cao, C. Tang, J. Liu, L.-L. Duan, Y. Huo, X. Shao, W. Hong and H.-L. Zhang, *J. Am. Chem. Soc.*, 2018, **140**, 6531–6535.

30   C. Huang, M. Jevric, A. Borges, S. T. Olsen, J. M. Hamill, J.-T. Zheng, Y. Yang, A. Rudnev, M. Baghernejad, P. Broekmann, A. U. Petersen, T. Wandlowski, K. V. Mikkelsen, G. C. Solomon, M. Brøndsted Nielsen and W. Hong, *Nat. Commun.*, 2017, **8**, 15436.

31   K. G. L. Pedersen, A. Borges, P. Hedegård, G. C. Solomon and M. Strange, *J. Phys. Chem. C*, 2015, **119**, 26919–26924.

32   F. Plasser, *J. Chem. Phys.*, 2020, **152**, 084108.